Preprint typeset in JINST style - HYPER VERSION

In-situ calibration of the single-photoelectron charge response of the IceCube photomultipliers

IceCube author list to be inserted... E-mail: analysis@icecube.wisc.edu

ABSTRACT: This article outlines the in-situ calibration of the single-photoelectron charge distributions for each of the Hamamatsu Photonics R7081-02 (MOD) photomultipliers in the IceCube Neutrino Observatory. The accurate characterization of the individual PMT charge distributions is important for event reconstruction and calibration. We discuss the single photoelectron identification procedure and how we extract the single-photoelectron charge distribution using a deconvolution of the multiple photoelectron charge distribution, and we examine various correlations between the shape of the single-photoelectron charge distribution and various hardware components. The time dependence of the individual PMT charge distributions is also investigated.

KEYWORDS: IceCube, single photoelectron, charge distribution, PMT.

Contents

---

1. Introduction

The IceCube Neutrino Observatory [1, 2] is a cubic-kilometer-sized array of 5,160 photomultiplier tubes (PMTs) buried in the Antarctic ice sheet, designed to observe high-energy neutrinos interacting with the ice [3]. In 2011, the IceCube Collaboration completed the installation of 86 vertical *strings* of PMT modules, eight of which were arranged in a denser configuration known as the DeepCore sub-array [4]. Each string in IceCube contains 60 digital optical modules (DOMs), which contain a single PMT each, as well as all required electronics [5]. The primary 78 strings (excluding DeepCore) are spaced 125 m apart in a hexagonal grid, with the DOMs extending from 1450 m to 2450 m below the surface of the ice sheet. The additional DeepCore strings (79-86) are positioned between the centermost strings in the detector, reducing the horizontal DOM-to-DOM distance in this region to 42 m and 72 m. The lower 50 DOMs on these strings are located in the deepest 350 m of the detector near the clearest ice, while the upper ten provide a cosmic ray veto extending down from 1900 m to 2000 m below the surface.

Each DOM consists of a 0.5" thick spherical glass pressure vessel that houses a single down-facing 10" PMT from Hamamatsu Photonics. The PMT is coupled to the glass housing with optical

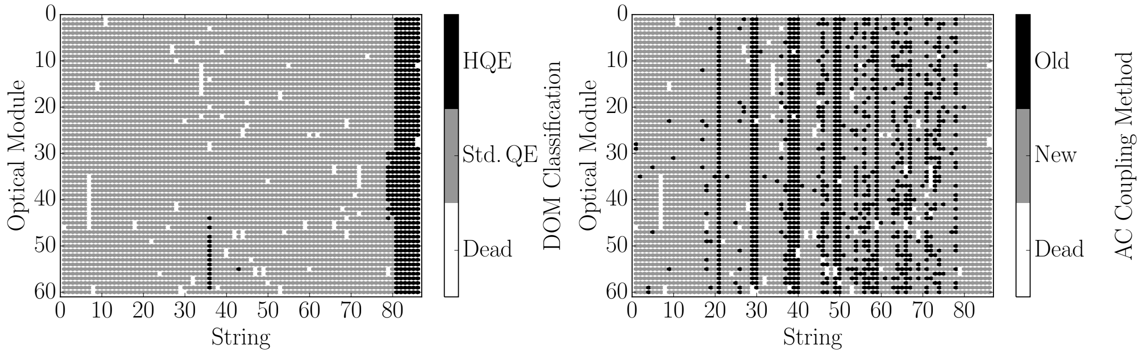

Figure 1. Left: A mapping of the HQE (black) and Standard QE DOMs (gray). Right: The version of AC coupling, old toroids (black) and new toroids (gray). DOMs that have been removed from service are shown in white.

gel and is surrounded by a wire mesh of mu metal to reduce the effect of the Earth's ambient magnetic field. The glass housing is transparent to wavelengths 350 nm and above [6].

Of the 5,160 DOMs, 4,762 house a R7081-02 Hamamatsu Photonics PMT, specified for wavelengths ranging from 300 nm to 650 nm, with peak quantum efficiency of 25% near 390 nm. These are classified as Standard Quantum Efficiency (Standard QE) DOMs. The remaining 398 DOMs are equipped with the Hamamatsu R7081-02MOD PMTs, which, having a peak quantum efficiency of 34% near 390 nm (36% higher efficiency than the Standard QE DOMs), are classified as High Quantum Efficiency (HQE) DOMs [4]. These DOMs are primarily located in DeepCore and on strings 36 and 43, as shown in the left side of Fig. 1.

The R7081-02 and R7081-02MOD PMTs have 10 dynode stages and are operated with a gain of 10^7 and high voltage around 1200 V. A typical amplified single photoelectron will generate a ~6 mV peak voltage at the input to the front-end amplifiers. The PMTs operate with the anodes at high voltage and the signal is AC coupled to the front-end amplifiers. There are two versions of AC coupling in the detectors, both of which use custom-designed wideband bifilar wound 1:1 toroidal transformers[1]. The locations of DOMs with the different versions of AC-coupling, new and old toroids, are shown on the right side of Fig. 1. The DOMs with the old toroids were designed with an impedance of 43 Ω, while the new toroids are 50 Ω [7]. All HQE DOMs are instrumented with the new toroids.

IceCube relies on two observables per DOM to reconstruct events: the total number of detected photons and their timing distribution. Both the timing and the number of photons are extracted from the digitized waveforms. This is accomplished by deconvolving the waveforms into a series of scaled single photoelectron pulses (so-called pulse series) and the integral of the individual pulses (divided by the load resistance) defines the observed charge. It will often be expressed in units of PE, or photoelectrons, which further divides the measured charge by the charge of a single electron times the nominal gain (10^7). Accurate characterization of the individual PMT charge distributions

[1] Conventional AC-coupling high-voltage ceramic capacitors can produce noise from leakage currents and impractical requirements on the capacitors in order to meet the signal droop and undershoot requirements. The toroidal transformer effectively acts as a high-pass filter with good signal fidelity at high frequencies. It also provides higher reliability than capacitive coupling and reduces the stored energy, which might cause damage if there is HV discharge in the system [6]. However, the toroidal-transformer AC coupling also introduces signal droop and undershoot.

is crucial for calibration and event reconstructions relying on charge information. The charge distribution can also be used to assess long-term detector performance and identify discrepancies between data and Monte Carlo. It is therefore critically important to accurately measure the single-photoelectron (SPE) charge distribution in order to understand the IceCube detector behavior.

When one or more photons produce a voltage at the anode sufficient to trigger the onboard discriminator (set via a DAC to approximately 1.3 mV, or equivalently to 0.25 PE), the signal acquisition process is triggered. The signal is fed into four parallel input channels. Three of the channels pass first through a 75 ns delay loop in order to capture the leading edge of the pulse and then into three high-speed (300 MSPS for 128 samples) 10-bit waveform digitizers (Analog Transient Waveform Digitizer, ATWD), each of which has a different level of amplification: 15.7 ± 0.6, 1.79 ± 0.06, and 0.21 ± 0.01 [7]. There are also three extra ATWDs on board each DOM: one is used for calibration and the other two operate in a ping-pong fashion to remove dead time associated with the readout. The signal to the fourth channel is first shaped and amplified and then fed into a 10-bit fast analog-to-digital converter (fADC) operating at a sampling speed of 40 MSPS. Further detail regarding the description of the DOM electronics can be found in Refs. [5, 8].

This article discusses the accurate determination of how individual DOMs collect charge in order to improve calibration and the detector description as used in the IceCube Monte Carlo simulation. It describes the procedure for determining the PMT's gain characteristics as seen in the SPE charge distributions using in-situ data from the IceCube detectors. The SPE charge distribution refers to the measured charge probability density function of the individual DOMs generated by the amplification of a pure sample of single photoelectrons. The extraction of the SPE charge distribution was recently made possible with the development of two pieces of software:

1. A specially-designed unbiased pulse selection was developed to reduce the multiple photoelectron (MPE) contamination while accounting for physical phenomena (e.g., late pulses, afterpulses, pre-pulses, and baseline shifts) and software-related effects (e.g., pulse splitting). This is further described in Sec. 2.1.

2. A fitting procedure was developed that separates the remaining MPE contamination from the SPE charge distribution by deconvolving the measured charged distribution. This is further described in Sec. 2.3.

By using in-situ data to determine the SPE charge distributions, we accurately represent the individual PMT response as a function of time, environmental conditions, software version and hardware differences, and we sample photons uniformly over the surface of the photocathode. This is beneficial since it also allows us to inspect the stability and long-term behavior of the individual DOMs, verify previous calibration, and correlate features with specific DOM hardware.

1.1 Single-photoelectron charge distributions

In an idealized scenario, a single photon produces a single photoelectron, which is then amplified by a known amount and the measured charge corresponds to 1 PE. However, there are many physical processes that create structure in the measured charge distributions. For example:

- **Statistical fluctuation due to cascade multiplication** [9]. At every stage of dynode amplification, there is a stochastic spread in the number of emitted electrons that make it to the next dynode. This in turn causes a spread in the measured charge after the gain stage of the PMT.

- **Photoelectron trajectory**. Some electrons may deviate from the favorable trajectory, reducing the number of secondaries produced at a dynode or the efficiency to collect them on the following dynode. This can occur at any stage, but it has the largest effect on the multiplication at the first dynode [10]. The trajectory of a photoelectron striking the first dynode will depend on many things, including where on the photocathode it was emitted, the uniformity of the electric field, the size and shape of the dynodes [9], and the ambient magnetic field [11, 12].

- **Late or delayed pulses**. A photoelectron can elastically or inelastically scatter off the first dynode. The scattered electron can then be re-accelerated to the dynode, creating a second pulse. The difference in time between the initial pulse and the re-accelerated pulse in the R7081-02 PMT was previously measured to be up to 70 ns [6, 13]. The two sub-pulses have lower charges, but the sum of the two tends to add up to the original charge. Collecting either the initial pulse or the late pulse will result in the charge being reconstructed in the low-PE region [14].

- **Afterpulses**. When a photoelectron or the secondary electrons produced during the electron cascade gain sufficient energy to ionize residual gas in the PMT, the positively charged ionized gas will be accelerated in the electric field towards the photocathode. Upon impact with the photocathode, electrons can be again released from the photocathode, creating what is called an afterpulse. For the R7081-02 PMTs, the timescale for afterpulses was measured to occur from 0.3 to 11 μs after the initial pulse, with the first prominent afterpulse peak occurring at approximately 600 ns [6]. The spread in the afterpulse time is dependent on the position of photocathode, the charge-to-mass ratio of the ion produced, and the electric potential distribution [15], whereas the size of the afterpulse is related to the momentum and species of the ionized gas and composition of the photocathode [16].

- **Pre-pulses**. If an incident photon passes through the photocathode without interaction and strikes one of the dynodes, it can eject an electron that is only amplified by the subsequent stages, resulting in a lower measured charge (lower by a factor of approximately 25). For the IceCube PMTs, the prepulses have been found to arrive approximately 30 ns before the signal from other photoelectrons from the photocathode [6].

- **MPE contamination**. When multiple photoelectrons arrive at the first dynodes within several nanoseconds of each other, they can be reconstructed by the software as a single, MPE pulse.

- **Electronic noise**. This refers to the fluctuations in the analog-to-digital converters (ATWDs and FADC) and ringing that arises from the electronics.

Beyond the physical phenomena above that modify the measured charge distribution, there is also a lower limit on the smallest charge that can be extracted. For IceCube, the discriminator limits the trigger pulse to be above approximately 0.25 PE, and subsequent pulses in the readout time window are subject to a software-defined threshold. The software threshold was set conservatively to avoid extracting pulses that originated from electronic noise. This threshold can be modified to gain access to lower charge pulses and will be discussed in Sec. 2.2.

The standard SPE charge distribution model used by the IceCube Collaboration, known as the TA0003 distribution [6], represented the above effects as the sum of an exponential plus a Gaussian. The exponential component represented charge of poorly amplified pulses and the Gaussian represented the spread in statistical fluctuations due to the cascade multiplication. The TA0003 distribution was previously used to describe all the PMTs in the IceCube detectors.

Recently, IceCube has performed several lab measurements using the R7081-02 PMTs with in-time laser pulses, demonstrating that the in-time charge distribution includes a steeply falling low-charge component below the discriminator threshold. To account for this, a new functional form including a second exponential was introduced. This form of the charge distribution $f(q)_{SPE} =$ Exp_1 + Exp_2 + Gaussian, is referred to as the *SPE template* in this article. Explicitly, it is:

$$f(q)_{SPE} = E_1 e^{-q/w_1} + E_2 e^{-q/w_2} + N e^{-\frac{(q-\mu)^2}{2\sigma^2}}, \tag{1.1}$$

where q represents the measured charge; E_1, E_2, and N represent normalization factors of each components; w_1 and w_2 are the exponential decay widths; and μ, σ are the Gaussian mean and width, respectively. This is the assumed functional shape of the SPE charge distributions and the components of Eq. 1.1 are determined in this article for all in-ice DOMs. IceCube defines 1 PE as the location of the Gaussian mean (μ) and calibrates the gain on the individual PMTs during the start of each season to meet this definition. The choice of where we define 1 PE is arbitrary, since linearity between the total charge collected and the number of incident photons is satisfied up to ~2 V [7]. This is because the average of the distribution is a set fraction of the Gaussian mean and the mean of a N-fold convolution is the sum of means. Any bias in the total observed charge can be absorbed into an efficiency term, such as the quantum efficiency.

1.2 IceCube datasets and software definitions

The largest contribution to the IceCube trigger rate comes from downgoing muons produced in cosmic ray induced showers [17]. Cosmic ray muons stopping in the detector cause the individual trigger rate to decrease at lower depths. Further, climate variations during the formation of the ice sheet caused depth-dependent changes in the optical properties of the ice. The optical properties also affect the trigger rate; in particular, the “dust layer" from 2100 to 2200 m below the surface is a region in the ice with relatively large scattering and absorption coefficients [18].

An induced signal in the PMT that passes through the AC coupling toroid located on the base of the PMT is compared to a discriminator threshold. If a DOM and its nearest or next to nearest neighbor observe a discriminator threshold crossing within a set time window, a *Hard Local Coincidence* (HLC) is initiated and the corresponding waveforms are sampled 128 times and read out on the three ATWDs.

After waveform digitization, there is a correction applied to remove the measured DC baseline offset. The signal droop and undershoot introduced by the toroidal transformer AC coupling is compensated for in software during waveform calibration by adding the expected temperature-dependent reaction voltage of the undershoot to the calibrated waveform. If the undershoot voltage drops below 0 ADC counts, the ADC values are zeroed and then compensated for once the waveform is above the minimum ADC input. Scaled single photoelectron pulse shapes (that take into account the version of the AC coupling) are then fit to the waveforms using software referred to as "WaveDeform" (waveform unfolding process), which determines the individual pulse time stamps and charges and populates a pulse series [19].

The pulse series used in this analysis come from two datasets provided by IceCube:

1. The **MinBias dataset.** This dataset records the full waveform readout of randomly-triggered HLC events at a rate that corresponds on average to 1/1000 events. The largest contribution to the IceCube trigger rate comes from downgoing muons produced in cosmic-ray-induced showers [17] and therefore is the largest signal component in this dataset. These muons tend to have small energies when they reach the detector, thus they produce minimal MPE contamination. The full waveform of these events allows us to extract the raw information about the individual pulses. This will be used to measure the individual PMT charge distributions.

2. The **BeaconLaunch dataset.** This is a forced triggered filter that is typically used to monitor the individual DOM baseline. It includes the full ATWD-window waveform readout. Since this dataset is forced-triggered, the majority of these waveforms represent baseline fluctuations with minimal contamination from the occasional coincidental pulse that makes it into the readout window. This dataset will be used to examine the noise contribution to the charge distributions. Note: when using this dataset, the weight of every pulse is multiplied by a factor of 28.4 to account for the livetime difference between the MinBias dataset and the BeaconLaunch dataset. Weight, in this context, refers to the number of photons in the MinBias dataset proportional to one photon in the BeaconLaunch dataset for which both datasets have the same equivalent livetime.

This analysis uses the full MinBias and BeaconLaunch datasets from IceCube seasons 2011 to 2016 (subsequently referred to as IC86.2011 to IC86.2016). Seasons in IceCube typically start in June of the labeled year and end approximately one year later. Calibration is performed at the beginning of each season.

2. Extracting the SPE templates

2.1 Single photoelectron pulse selection

The pulse selection is the method used to extract candidate, unbiased, single photoelectron pulses from data while minimizing the MPE contamination. It avoids collecting afterpulses, rejects late pulses from the trigger, reassembles late pulses, accounts for the discriminator threshold, reduces the effect of droop and baseline undershoot, and gives sufficient statistics to perform a season-to-season measurement. An illustrative diagram of the pulse selection is shown in the left side of Fig. 2, while a description of the procedure is detailed below.

We restrict the pulse selection to only extract information from waveforms in which the trigger pulse does not exceed 10 mV and no subsequent part of the waveform exceeds 20 mV. This reduces the effect of the baseline undershoot due to the AC coupling or other artifacts from large pulses.

In order to trigger a DOM, the input to the front-end amplifiers must exceed the discriminator threshold. To avoid the selection bias of the discriminator trigger, we ignore the trigger pulse as well as the entire first 100 ns of the time window. Ignoring the first 100 ns has the added benefit of also removing late pulses that could be attributed to the triggering pulse. To ensure we are not accepting afterpulses into the selection, we also enforce the constraint that the pulse of interest (POI) is within the first 375 ns of the ATWD time window. This also allows us to examine the waveform up to 50 ns after the POI. In the vicinity of the POI, we check that WaveDeform did not reconstruct any pulses up to 50 ns prior to the POI, or 100 to 150 ns after the POI (the light gray region of Fig. 2 (left)). This latter constraint is to reduce the probability of accidentally splitting a late pulse in the summation window.

If a pulse is reconstructed between 100 and 375 ns after the time window is opened and the voltage criteria are met, it is accepted as a candidate photoelectron and several checks are performed on the waveform prior to and after the pulse. The first check is to ensure that the waveform is near the baseline just before the rising edge of the POI. This is accomplished by ensuring that the waveform does not exceed 1 mV, 50 to 20 ns prior to the POI, and eliminates cases where the POI is a late pulse. We also ensure the waveform returns to the baseline by checking that no ADC measurement exceeds 1 mV, 100 to 150 ns after the POI. These constraints are illustrated as the horizontal red dotted lines and black arrows in the left side of Fig. 2.

If all the above criteria are met, we sum the reconstructed charges from the POI time, given by WaveDeform, to +100 ns (the dark gray area in Fig. 2 (left)). This ensures that any nearby pulses are either fully separated or fully added. WaveDeform may occasionally split an SPE pulse into

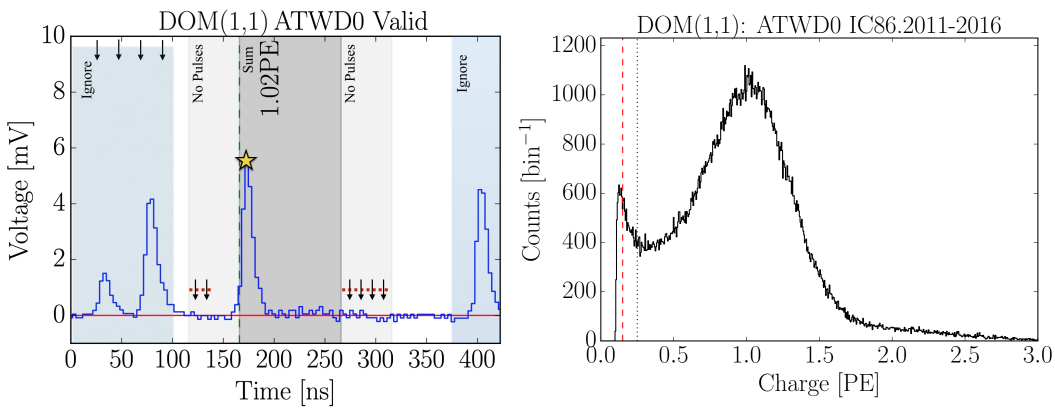

Figure 2. Left: An illustrative diagram of the pulse selection criteria for selecting a high-purity and unbiased sample of single photoelectrons. The digitized ATWD waveform is shown in blue. The pulse of interest is identified with a yellow star. This example waveform was triggered by a small pulse at 25 ns (recall that the delay board allows us to examine the waveform just prior to the trigger pulse), followed by a potential late pulse at 70 ns. At 400 ns, we see a pulse in the region susceptible to afterpulses. Waveform voltage checks are illustrated with arrows, and various time windows described in the text are drawn with semi-opaque regions. The POI is reported to have a charge of 1.02 PE, given by WaveDeform, and would pass the pulse selection criteria. Right: The collected charges from string 1, optical module 1 (DOM 1,1), from the MinBias dataset collected from IC86.2011 to IC86.2016 that pass the pulse selection. The discriminator threshold at 0.25 PE is represented as a dotted black vertical line. For visual purposes, a vertical dashed red line is also included at 0.15 PE.

multiple smaller pulses, therefore it is always critical to perform a summation of the charge within a window. The 100 ns summation also means that the pulse selection will occasionally accept MPE events.

2.2 Characterizing the low-charge region

Fig. 2 (right) shows the charge distributions of the selected pulses that pass the single photoelectron pulse selection for string 1, optical module 1, DOM(1,1). In the low-charge region (below 0.25 PE), we see a second threshold at approximately 0.13 PE. This is a software-defined threshold that comes from a gradient-related termination condition in WaveDeform. The threshold was set to avoid electronic noise being interpreted as PMT pulses and contaminating the low-charge region.

The steeply falling component of the region from 0.13 PE to 0.25 PE is in agreement with the in-time laser tests mentioned in Sec. 1.1 and emphasizes the importance of collecting data below the discriminator. This section will assess the noise contribution to this region and examine the effect on the charge distribution and noise contribution by lowering the WaveDeform threshold.

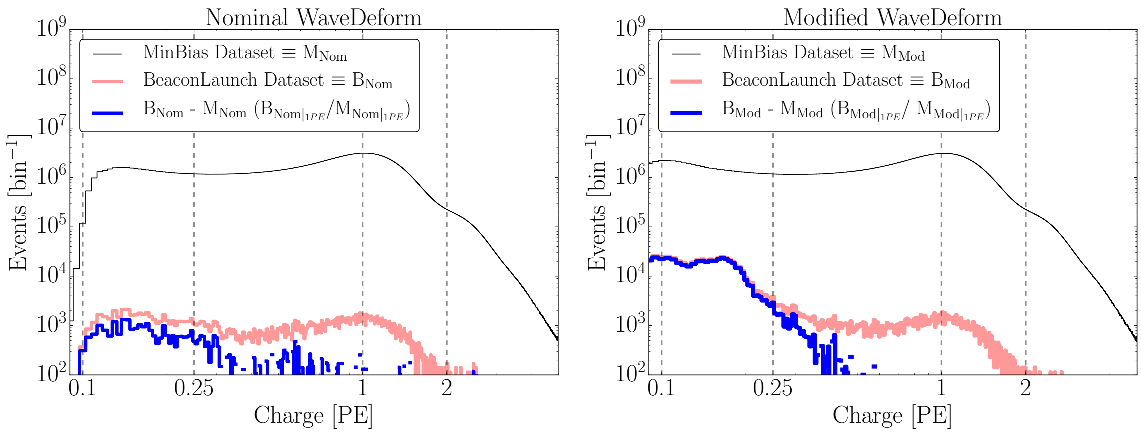

Figure 3. The cumulative charge distributions of all DOMs for the MinBias and BeaconLaunch datasets. The blue histogram shows the expected contribution from noise. This was found by subtracting the shape of the MinBias dataset from the BeaconLaunch dataset. Left: The charge distributions for the standard WaveDeform settings. Right: The charge distributions for the modified WaveDeform settings.

Fig. 3 (left) shows the charge distributions for the MinBias (black) and the BeaconLaunch (red) datasets using the default settings of WaveDeform. As mentioned in Sec. 1.2, occasionally a photoelectron will be coincident with the forced BeaconLaunch time window. These charges populate a SPE distribution. Subtracting the shape of the MinBias charge distribution from the BeaconLaunch dataset yields an estimate of the amount of electronic noise contamination (blue). The bin with the largest signal-to-noise ratio (SNR) above 0.1 PE was found to have a SNR of 0.0013. The SNR for the full distribution was found to be 0.0005. Fig. 3 (right) shows the same data after lowering the WaveDeform threshold. Correspondingly, the bin with the largest SNR was found to have a SNR of 0.017, whereas the total SNR was found to be 0.0015.

The modified WaveDeform datasets show a minimal increase in the contribution of noise to the low-charge region. From this, we are able to extract charge information down to approximately

0.10 PE and improve the overall description of the charge distribution below the discriminator. This will help constrain the values defining Exp_1.

2.3 Fitting procedure

The fit assumes that there is a negligible three-PE contribution, which is justified by the lack of statistics in the 3 PE region as well as the significant rate difference between the 1 PE and 2 PE region, as shown in Fig. 2 (right). The 2 PE charge distribution is assumed to be the SPE charge distribution convolved with itself [20]. A python-based piece of software called the "convolutional fitter" is used to determine the components of Eq. 1.1 from the measured charge distribution that includes the MPE contamination.

The Exp_2 component, as well as the Exp_1, of Eq. 1.1 represent poorly amplified photoelectrons, and we do not allow it to extend beyond the high-charge region of the Gaussian component. In particular, we include a constraint on the the parameter w_2 to ensure that it falls off with the Gaussian component:

$$w_2 < \frac{\mu + 2\sigma}{4 - \mathrm{Ln}(N/E_2)}. \tag{2.1}$$

This equation was found by setting the Exp_2 to be $1/\mathrm{e}^2$ that of the Gaussian component at two sigma (the Exp_1 is neglected from this equation since it falls off in the low-charge region). Eq. 2.1 is used as a constraint during the fit to the charge distributions.

Pulses that fall below the WaveDeform threshold and are not reconstructed contribute to an effective efficiency of the individual DOMs. This analysis assumes the same shape of the steeply falling exponential component (Exp_1) for all DOMs in the detector to avoid large fluctuations in the individual DOM efficiencies. The modified WaveDeform data will strictly be used to determine the Exp_1 component. Specifically, using the modified WaveDeform, we will background-subtract the BeaconLaunch distribution from the MinBias data, fit the resulting distribution to determine the components of Eq. 2.1, and use only the measured shape and normalization of Exp_1 in all subsequent unmodified WaveDeform fits.

As described in Sec. 1.1, the Gaussian mean (μ) is used to determine the gain setting for each PMT. Therefore, it is particularly important that the fit quality in this region accurately describes the data. While fitting to the full charge distribution improves the overall fit agreement, the mismatch between the chosen functional form (Eq. 1.1) and a true SPE charge distribution can cause the Gaussian component to pull away from its ideal location. To compensate for this, the convolutional fitter prioritizes fitting to the data around the Gaussian mean. This is accomplished by first fitting to the full distribution to get an estimate of the Gaussian mean location. Then, the statistical uncertainty is reduced in the region ± 0.15 PE around the original estimated Gaussian mean, and the distribution is re-fitted.

Upon fitting the MinBias data with the predetermine values for Exp_1, the residual of each fit is calculated by measuring the percentage difference between the fit and the data. The average residual will then be used as a global scaling factor for all SPE templates to account for the difference between the chosen model (Eq. 2.1) and the actual data.

All the DOMs with "failed fits" are not included in this article. A DOM is classified as having a failed fit if it does not pass one of the validity checks on the data requirements (e.g. number of valid pulses) or goodness of fit. The majority of these DOMs have been removed from service (approximately 109 DOMs) and the remaining approximately 6 DOMs are known to have various issues. In the IceCube MC simulation chain, these DOMs are assigned the average SPE template.

2.4 SPE template fit results

Using the background-subtracted modified WaveDeform dataset, the Exp_1 component was determined by fitting the distribution from 0.1 PE to 3.5 PE. The result of the fit yielded $E_1 = 6.9 \pm 1.5$ and $w_1 = 0.032 \pm 0.002$ PE. The shape of Exp_1 is then used to describe the low-PE charge region for all subsequent fits.

Using the MinBias dataset with the measured values of Exp_1, the SPE templates are extracted for every DOM, separately for each IceCube season (IC86.2011 to IC86.2016). The fit range for Exp_2 and the Gaussian components is selected to be between 0.15 PE and 3.5 PE. An average fit was also performed on the cumulative charge distribution, in which all the data for a given DOM was summed together (labeled as "AVG").

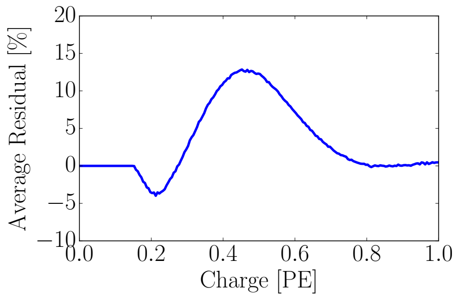

Figure 4. The measured average residual of the SPE templates fit.

We can divide the DOMs into subsets of hardware differences: the HQE DOMs with the new toroids, the Standard QE DOMs with the new toroids, and the Standard QE DOMs with the old toroids. The mean value and standard error of the IC86.AVG fit parameters, excluding Exp_1, for the subset of hardware differences are listed in Table 1. The average residual for all DOMs from 0 to 1 PE is shown in Fig. 4.

Hardware Configuration	Exp_2 Amp. (E_2)	Exp_2 Width (w_2)	Gaus. Amp. (N)	Gaus. Mean (μ)	Gaus. Width (σ)
HQE / New Toroid	0.644 ± 0.003	0.405 ± 0.003	0.715 ± 0.002	1.0202 ± 0.0010	0.311 ± 0.001
Std. QE / New Toroids	0.566 ± 0.001	0.403 ± 0.001	0.751 ± 0.001	1.0238 ± 0.0004	0.316 ± 0.001
Std. QE / Old Toroids	0.525 ± 0.002	0.420 ± 0.002	0.813 ± 0.002	1.0074 ± 0.0007	0.294 ± 0.001

Table 1. The average values and standard error of each fit parameter for the subset of hardware configurations listed in the first column.

An example fit is shown in Fig. 5 for the cumulative charge distribution for DOM (1,1). The collected charge distribution is shown in the black histogram, while the convolutional fit is shown as the black line (multiplied by the residual). The extracted SPE template (also multiplied by the residual) for this DOM is shown in blue.

3. Discussion

3.1 Correlations between fit parameters and DOM hardware differences

It is evident from the data provided in Table 1 that the average shape of the SPE templates is dependent on the DOM hardware. Most notably, when we examine the subset of DOMs instrumented

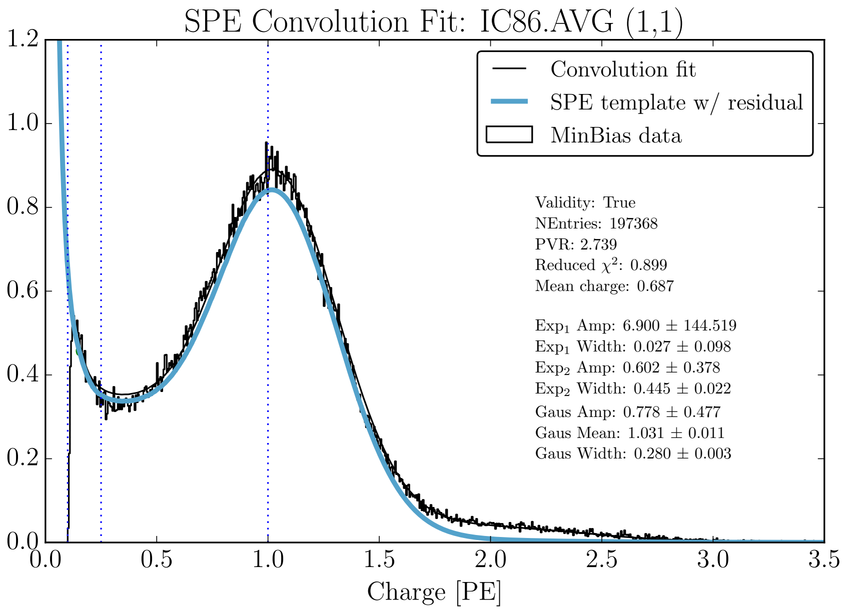

Figure 5. An example fit including the residual correction for DOM(1,1) using the WaveDeform dataset for seasons IC86.2011 to IC86.2016. The result from the convolutional fitter is shown as a solid black line. The extracted SPE template is shown blue.

with the new toroids, the average HQE DOM were found to have a particularly larger E_2 component ($13.8 \pm 0.6\%$) and smaller Gaussian amplitude ($-4.77 \pm 0.03\%$). Consequently, the average HQE peak-to-valley ratio is measured to be 2.322 ± 0.013, corresponding to $-12.12 \pm 0.06\%$ lower than the average Standard QE DOMs. Also, interestingly, the mean charge of the average HQE DOM was found to be $-3.34 \pm 0.01\%$ lower than for the Standard QE DOMs. IceCube compensates for the change in the mean measured charge in simulation, by increasing the HQE DOM efficiency by the equivalent amount. This ensures that the total amount of charge collected by the HQE DOMs remains the same prior to, and after, inserting the SPE templates into simulation.

Similarly, using only the subset of Standard QE DOMs, the SPE templates comparing the method of AC coupling were found to have a measurably different shapes. The average Gaussian amplitude and width for the DOMs instrumented with the old toroids were found to be $+8.31 \pm 0.01\%$ and $-6.80 \pm 0.03\%$, respectively. With these differences, we find a peak-to-valley ratio of 2.643 ± 0.008 for the old toroid DOMs and 3.012 ± 0.012 for the new toroid DOMs. The average Gaussian mean of the fit for the DOMs with the old toroids was also found to be $-1.6 \pm 0.1\%$ lower than those with the new toroids. This corresponds proportionally to a change in the expected gain. The mean charge, however, between these two hardware configurations remains very similar ($-0.346 \pm 0.001\%$).

Although the DOMs instrumented with the old toroids were deployed into the ice earlier than those with the new toroids, the differences above is still noted when examining individual deployment years; therefore, the shape differences are not attributed to the change in the DOM behavior over time. The DOMs with the old toroids were the first PMTs to be manufactured by Hamamatsu,

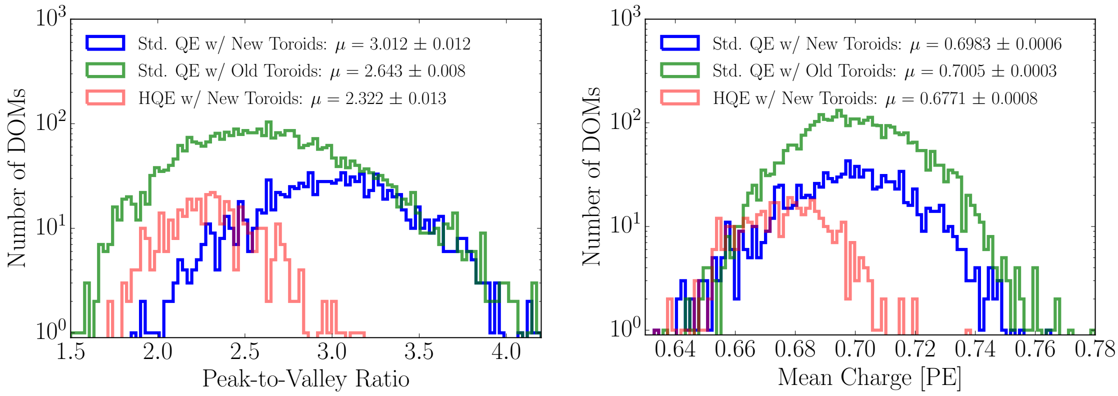

Figure 6. Comparison between the R7081-02MOD HQE DOMs and standard R7081-02 DOMs. Left: The peak-to-valley ratio for the two subsets of quantum efficiencies. Right: The mean charge of the individual DOM SPE templates.

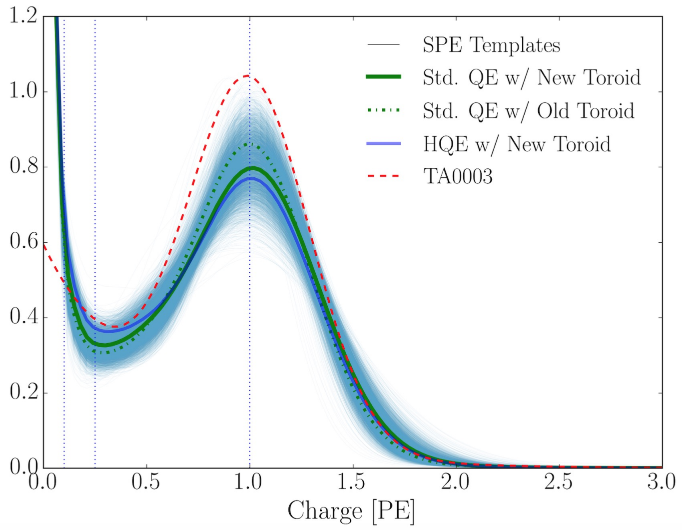

Figure 7. A comparison between the SPE templates (light blue band) and the TA0003 (dashed red line) distribution. The average SPE template for the Standard QE and HQE DOMs is shown as the thick blue and green lines, respectively. The SPE templates include the residual correction, and all curves are normalized.

so this difference may also be attributed to a gradual change in the process parameters over the course of PMT manufacturing, i.e. a change in the production procedure rather than the actual AC coupling version. It is also possible that the differences originate from the transfer function that models a single photoelectron waveform used in WaveDeform.

Fig. 6 shows the distribution of the measured peak-to-valley ratios and mean charge for the three different subsets of DOM hardware.

Fig. 7 illustrates the average shape differences in the measured SPE templates between the HQE DOM with the new toroids (thick blue line), Standard QE with the new toroids (thick green line), Standard QE with the old toroids (dash-dot green line), compared to the measured SPE templates from the AVG charge distributions (think blue lines). The figure also shows how the TA0003 distribution compares to this recent measurement. The shape difference in the TA0003 is attributed to better control of the low-charge region, the difference in functional form (described in Section 1.1), and the fact that the SPE templates sample uniformly over the entire photocathode at random incident angles.

3.2 Fitting parameters variation over time

The SPE templates were extracted for each IceCube season independently to investigate the time dependence of the fit parameters. For every DOM in the detector, the change over time of each fit parameter (excluding Exp_1) was calculated. Fig. 8 shows the change in a given fit parameter, relative to the mean value, per year. The measured distribution was found to be consistent with statistically scrambling the yearly measurements. The average of each fit parameters are found to deviate less than 0.1%, which is in agreement with the stability checks performed in Ref. [7]. This observation holds for the individual subset of DOMs with different hardware configurations as well.

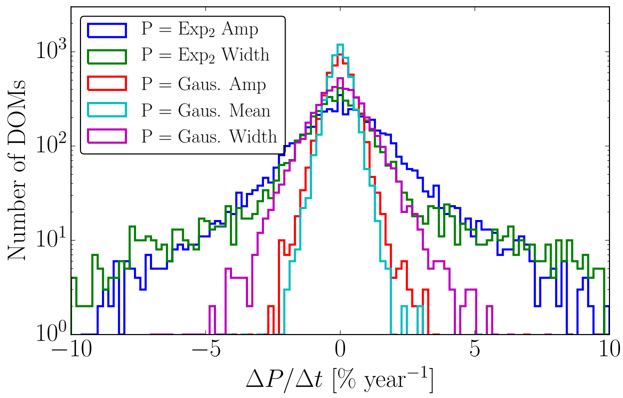

Figure 8. The change in the individual DOM fitted parameters over time, represented as percentage deviation from the mean fit parameter value.

3.3 Quantifying observable changes when modifying the PMT charge distributions

Changing the assumed gain response in simulation, as deduced from data, has different implications depending on the typical illumination level present in different analyses. These differences are outlined in the following discussion.

The PMT response is described by a combination of a "bare" efficiency, η_0, and a normalized charge response function, $f(q)$. The bare efficiency represents the fraction of arriving photons that result in any nonzero charge response, including those well below the discriminator threshold. The normalization condition is:

$$\int_0^{\mathrm{inf}} f(q)dq = 1. \tag{3.1}$$

Generally, $f(q)$ and η_0 have to be adjusted together to maintain agreement with a quantity known from lab or in-ice measurements, such as the predicted number of pulses above threshold for a dim source.

Dim source measurements Where light levels are low enough, sub-discriminator pulses do not contribute any observed charge because they do not satisfy the trigger threshold, and the probability of two photons arriving together is negligible. Given some independent way of knowing the number of arriving photons, a lab or in-ice measurement determines the trigger fraction above threshold $\eta_{0.25}$ and/or the average charge over threshold $Q_{0.25}$, either of which can be used to constrain the model as follows:

$$\eta_{0.25} = \eta_0 \int_{0.25q_{pk}}^{\inf} f(q)dq \tag{3.2}$$

$$Q_{0.25} = \eta_0 \int_{0.25q_{pk}}^{\inf} qf(q)dq \tag{3.3}$$

Here, the discriminator threshold is assumed to be 0.25 times the peak position q_{pk}. It is also useful to multiply observed charges by q_{pk}, since we set each PMT gain by such a reference, and then a measurement constraint would be stated in terms of $Q_{0.25}/q_{pk}$.

Semi-bright source measurements Once the ATWD window is open, subsequent pulses are not limited by the discriminator threshold. WaveDeform introduces a software termination condition at 0.1 PE (described at the end of Section 2.1). The average charge of an individual pulse that arrives within the time window is:

$$Q_{0.10} = \eta_0 \int_{0.10q_{pk}}^{\inf} qf(q)dq \tag{3.4}$$

Bright source measurements For light levels that are large, the trigger is satisfied regardless of the response to individual photons, and the total charge per arriving photon therefore includes contributions below both the discriminator and the WaveDeform thresholds:

$$Q_0 = \eta_0 \int_{0}^{\inf} qf(q)dq \tag{3.5}$$

As such, the total charge is directly proportional to the average charge of the SPE template, having a strong dependence on Exp_1.

3.3.1 Model comparison

When the charge distribution model is changed in a way that preserves agreement with the measured $\eta_{0.25}$ or $Q_{0.25}/q_{pk}$, i.e., η_0 is adjusted properly for changes in $f(q)$, the physical effect can be summarized by the change in the bright-to-dim ratios $Q_0/Q_{0.25}$, and $Q_0/Q_{0.10}$. Conveniently, these ratios depend only on the shape of $f(q)$. Table 2 compares these ratios in terms of the TA0003 charge distribution and the SPE templates described here. It is shown that there are sub-percent level differences in the physically-observable bright-to-dim ratios.

3.4 SPE templates in simulation

The IceCube Monte Carlo simulation chain assigns a charge to every photoelectron generated at the surface of the photocathode. The charge is determined by sampling from a normalized charge distribution probability density function. A comparison between describing the charge distribution using the SPE templates and the TA0003 distribution follows.

Model	Detector	$Q_0/Q_{0.25}$	$Q_0/Q_{0.10}$	$\eta_{0.25}/Q_{0.25}$
TA0003	All DOMs	1.017	1.0031	1.05
SPE Templates	HQE + New Toroids	1.021±0.002	1.0041±0.0004	1.05±0.02
	Std. QE + New Toroids	1.018±0.002	1.0035±0.0005	1.03±0.02
	Std. QE + Old Toroids	1.017±0.002	1.0033±0.0005	1.05±0.02

Table 2. The distribution in bright-to-dim ratios for the previous charge distribution (TA0003) and the individual DOM SPE templates for the IceCube and DeepCore detectors.

Two simulation sets consisting of the same events were processed through the IceCube Monte Carlo simulation chain to the final analysis level of an update to the IC86.2011 sterile neutrino analysis [21]. Here, the events that pass the cuts are >99.9% pure upgoing (a trajectory oriented upwards relative to the horizon) secondary muons produced by charged current muon neutrino/antineutrino interactions. The muon energy range of this event selection is between approximately 500 GeV and 10 TeV.

Fig. 9 (left) shows the distribution of the total measured charge in a single DOM during each event. The data is shown for the full IC86.2012 season but is statistically equivalent to any of the other seasons. The simulation set using the TA0003 charge distribution is shown in orange, and that using the SPE templates is shown in blue. The bottom of the plot shows the ratio of the measured quantity relative to data. Fig. 9 (right) shows the distribution of the measured total charge on a DOM (after noise removal) divided by the number of channels, or DOMs, that participated in the event. Both plots in Fig. 9 have been normalized such that the area under the histograms is the same.

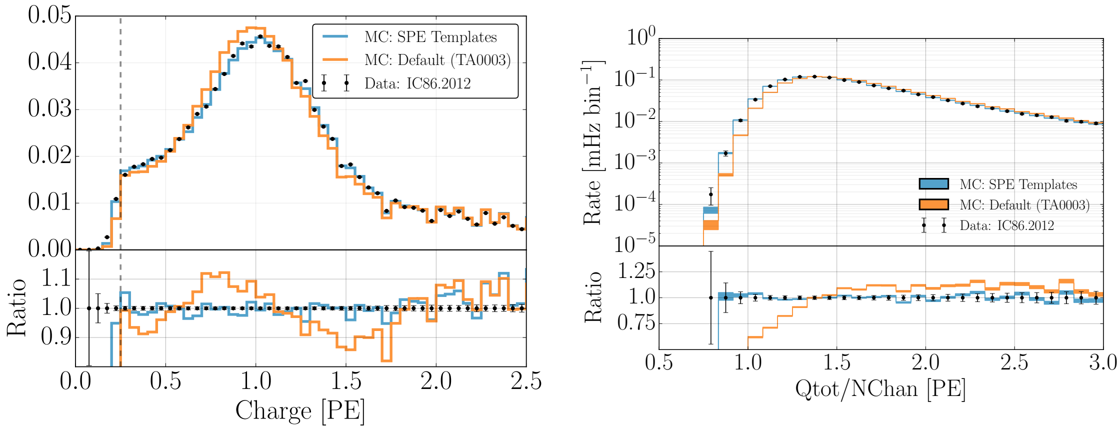

Figure 9. A comparison between the SPE templates (blue) and the TA0003 (orange) model for describing the SPE charge distribution in Monte Carlo. The simulation is compared to the 2012 IceCube season. Left: The total measured charge per DOM, per event at analysis level. Right: The distribution of the total measured charge of an event divided by the number of DOMs that participated in the event.

The SPE templates clearly improve the overall MC description of these two variables. IceCube includes a systematic uncertainty in all analyses, which scales the DOM efficiency to account for effects that change the total observed charge. This systematic compensates for the overall mean charge shift introduced using the SPE templates; however, the SPE templates now introduce DOM-to-DOM differences. This is not expected to change the IceCube physics results since analyses are sensitive to the overall detector performance rather than the individual DOM variations.

3.5 SPE templates for calibration

The gain setting on each DOM is calibrated at the beginning of the season such that the Gaussian mean charge distribution corresponds to a gain of 10^7, or equivalently 1 PE. Since the method used to extract the Gaussian mean described in this article is different from the previous method used for calibration of the DOMs, the total measured charge from a DOM is expected to change with the updated calibration.

The Gaussian mean component of the fit of every year is found to be on average $2.00 \pm 0.03\%$ higher than unity with a standard deviation of 3.54%, corresponding to a systematic overestimation of the measured charge in the detector. This correction to the measured charge can be implemented retroactively by dividing the reported charge from WaveDeform by the corresponding Gaussian mean for a given DOM. Alternatively, the MC can account for this difference by simply inserting the SPE templates with Gaussian mean matching the values found in the data. Both of these solutions will be used in future IceCube data/MC production.

4. Conclusion

This article outlines the procedure used for collecting a high purity sample of single photoelectron charges for each of the in-ice DOMs in IceCube. Multiple photoelectron contamination was removed under the assumption that it is represented by the convolution of the SPE distribution multiple times.

The SPE templates were extracted for each season in the IceCube detector and investigated for time dependent behaviour and correlations with hardware-related features. No significant time dependence in any of the fitted parameters over the investigated seasons was observed, in agreement with Ref. [7]. Variations in the fit parameters were found to be consistent with statistical fluctuations. The HQE DOMs were found to have a smaller peak-to-valley ratio than the Standard QE DOMs, as well as an overall $-3.34 \pm 0.01\%$ lower mean charge. It was also found that the DOMs instrumented with the old toroids used for AC coupling had narrower and larger Gaussian component corresponding resulting in an increased peak-to-valley ratio of $14.0 \pm 0.6\%$.

The SPE templates were implemented into the MC simulation production chain and the results were compared to the default PMT charge distribution (TA0003). A significant improvement in the description of the low-level variables, total charge per DOM and total charge per event over the number of channels, was shown. After accounting for SPE templates, the effect on physics analysis, however, as shown by the bright-to-dim ratios, is expected to be minimal.

The new method for extracting the calibration constant that determines the gain setting on each of the PMTs (the Gaussian mean of the fit) has been revised and shows that the average gain was $2.00 \pm 0.03\%$ larger than expected. The SPE templates account for this shift in simulation. Previous physics analyses are not expected to be impacted by this since IceCube includes a systematic uncertainty that scales the bare efficiency of the DOMs with a prior defined sufficiently large to absorb this effect. Future reprocessing of the IceCube data will take this shift into account.

Acknowledgments

We acknowledge the support from the following agencies: U.S. National Science Foundation - Office of Polar Programs, U.S. National Science Foundation - Physics Division, University of Wisconsin Alumni Research Foundation, the Grid Laboratory Of Wisconsin (GLOW) grid infrastructure at the University of Wisconsin - Madison, the Open Science Grid (OSG) grid infrastructure; U.S. Department of Energy, and National Energy Research Scientific Computing Center, the Louisiana Optical Network Initiative (LONI) grid computing resources; Natural Sciences and Engineering Research Council of Canada, WestGrid and Compute/Calcul Canada; Swedish Research Council, Swedish Polar Research Secretariat, Swedish National Infrastructure for Computing (SNIC), and Knut and Alice Wallenberg Foundation, Sweden; German Ministry for Education and Research (BMBF), Deutsche Forschungsgemeinschaft (DFG), Helmholtz Alliance for Astroparticle Physics (HAP), Research Department of Plasmas with Complex Interactions (Bochum), Germany; Fund for Scientific Research (FNRS-FWO), FWO Odysseus programme, Flanders Institute to encourage scientific and technological research in industry (IWT), Belgian Federal Science Policy Office (Belspo); University of Oxford, United Kingdom; Marsden Fund, New Zealand; Australian Research Council; Japan Society for Promotion of Science (JSPS); the Swiss National Science Foundation (SNSF), Switzerland; National Research Foundation of Korea (NRF); Villum Fonden, Danish National Research Foundation (DNRF), Denmark.

References

[1] J. Ahrens *et al.*, “Icecube preliminary design document,” *URL: http://www. icecube. wisc. edu/science/publications/pdd*, 2001.

[2] A. Achterberg, M. Ackermann, J. Adams, J. Ahrens, K. Andeen, D. Atlee, J. Baccus, J. Bahcall, X. Bai, B. Baret, *et al.*, “First year performance of the icecube neutrino telescope,” *Astroparticle Physics*, vol. 26, no. 3, pp. 155–173, 2006.

[3] I. Collaboration *et al.*, “Evidence for high-energy extraterrestrial neutrinos at the icecube detector,” *Science*, vol. 342, no. 6161, p. 1242856, 2013.

[4] R. Abbasi, Y. Abdou, T. Abu-Zayyad, M. Ackermann, J. Adams, J. Aguilar, M. Ahlers, M. Allen, D. Altmann, K. Andeen, *et al.*, “The design and performance of icecube deepcore,” *Astroparticle physics*, vol. 35, no. 10, pp. 615–624, 2012.

[5] R. Abbasi, M. Ackermann, J. Adams, M. Ahlers, J. Ahrens, K. Andeen, J. Auffenberg, X. Bai, M. Baker, S. Barwick, *et al.*, “The icecube data acquisition system: Signal capture, digitization, and timestamping,” *Nuclear Instruments and Methods in Physics Research Section A: Accelerators, Spectrometers, Detectors and Associated Equipment*, vol. 601, no. 3, pp. 294–316, 2009.

[6] R. Abbasi, Y. Abdou, T. Abu-Zayyad, J. Adams, J. Aguilar, M. Ahlers, K. Andeen, J. Auffenberg, X. Bai, M. Baker, *et al.*, “Calibration and characterization of the icecube photomultiplier tube,” *Nuclear Instruments and Methods in Physics Research Section A: Accelerators, Spectrometers, Detectors and Associated Equipment*, vol. 618, no. 1-3, pp. 139–152, 2010.

[7] M. Aartsen *et al.*, “The icecube neutrino observatory: Instrumentation and online systems, jinst 12 (03)(2017) p03012,” *arXiv preprint arXiv:1612.05093*, pp. 1748–0221.

[8] R. Stokstad, “Design and performance of the icecube electronics,” 2005.

[9] Hamamatsu, “Resources: Basics and applications,” *URL: https://www.hamamatsu.com/resources/pdf/etd/PMT_handbook_v3aE.pdf*, 2018.

[10] Hamamatsu, “Handbook resources, chapter 4,” *URL: https://www.hamamatsu.com/resources/pdf/etd/PMT_handbook_v3aE-Chapter4.pdf*, 2018.

[11] J. Brack, B. Delgado, J. Dhooghe, J. Felde, B. Gookin, S. Grullon, J. Klein, R. Knapik, A. LaTorre, S. Seibert, *et al.*, “Characterization of the hamamatsu r11780 12 in. photomultiplier tube,” *Nuclear Instruments and Methods in Physics Research Section A: Accelerators, Spectrometers, Detectors and Associated Equipment*, vol. 712, pp. 162–173, 2013.

[12] E. Calvo, M. Cerrada, C. Fernández-Bedoya, I. Gil-Botella, C. Palomares, I. Rodríguez, F. Toral, and A. Verdugo, “Characterization of large-area photomultipliers under low magnetic fields: Design and performance of the magnetic shielding for the double chooz neutrino experiment,” *Nuclear Instruments and Methods in Physics Research Section A: Accelerators, Spectrometers, Detectors and Associated Equipment*, vol. 621, no. 1-3, pp. 222–230, 2010.

[13] F. Kaether and C. Langbrandtner, “Transit time and charge correlations of single photoelectron events in r7081 photomultiplier tubes,” *Journal of Instrumentation*, vol. 7, no. 09, p. P09002, 2012.

[14] B. Lubsandorzhiev, P. Pokhil, R. Vasiljev, and A. Wright, “Studies of prepulses and late pulses in the 8" electron tubes series of photomultipliers,” *Nuclear Instruments and Methods in Physics Research Section A: Accelerators, Spectrometers, Detectors and Associated Equipment*, vol. 442, no. 1-3, pp. 452–458, 2000.

[15] K. Ma, W. Kang, J. Ahn, S. Choi, Y. Choi, M. Hwang, J. Jang, E. Jeon, K. Joo, H. Kim, *et al.*, "Time and amplitude of afterpulse measured with a large size photomultiplier tube," *Nuclear Instruments and Methods in Physics Research Section A: Accelerators, Spectrometers, Detectors and Associated Equipment*, vol. 629, no. 1, pp. 93–100, 2011.

[16] S. Torre, T. Antonioli, and P. Benetti, "Study of afterpulse effects in photomultipliers," *Review of scientific instruments*, vol. 54, no. 12, pp. 1777–1780, 1983.

[17] M. Aartsen, K. Abraham, M. Ackermann, J. Adams, J. Aguilar, M. Ahlers, M. Ahrens, D. Altmann, T. Anderson, M. Archinger, *et al.*, "Characterization of the atmospheric muon flux in icecube," *Astroparticle physics*, vol. 78, pp. 1–27, 2016.

[18] M. Aartsen, R. Abbasi, Y. Abdou, M. Ackermann, J. Adams, J. Aguilar, M. Ahlers, D. Altmann, J. Auffenberg, X. Bai, *et al.*, "Measurement of south pole ice transparency with the icecube led calibration system," *Nuclear Instruments and Methods in Physics Research Section A: Accelerators, Spectrometers, Detectors and Associated Equipment*, vol. 711, pp. 73–89, 2013.

[19] M. Aartsen, R. Abbasi, M. Ackermann, J. Adams, J. Aguilar, M. Ahlers, D. Altmann, C. Arguelles, J. Auffenberg, X. Bai, *et al.*, "Energy reconstruction methods in the icecube neutrino telescope," *Journal of Instrumentation*, vol. 9, no. 03, p. P03009, 2014.

[20] R. Dossi, A. Ianni, G. Ranucci, and O. J. Smirnov, "Methods for precise photoelectron counting with photomultipliers," *Nuclear Instruments and Methods in Physics Research Section A: Accelerators, Spectrometers, Detectors and Associated Equipment*, vol. 451, no. 3, pp. 623–637, 2000.

[21] M. Aartsen, K. Abraham, M. Ackermann, J. Adams, J. Aguilar, M. Ahlers, M. Ahrens, D. Altmann, K. Andeen, T. Anderson, *et al.*, "Searches for sterile neutrinos with the icecube detector," *Physical review letters*, vol. 117, no. 7, p. 071801, 2016.